Geochemical Perspectives Letters

© 2024 The Authors
Published by the European Association of Geochemistry

The extent of liquid immiscibility in planetesimal cores

G.D. Bromiley, M. Varnam, H. Terasaki, T. Komabayashi, J. Barosch

Supplementary Information

The Supplementary Information includes:

- Methodology
- Results from super-liquidus experiments
- Modelling planetesimal core compositions
- Tables S-1 to S-4
- Figure S-1 and S-2
- Supplementary Information References

Methodology

Starting materials for superliquidus experiments

Starting mixes were prepared from high purity Fe (99.9), Ni (99.9), FeS (99.9), Fe_3P (99.5), and diamond powders, based on a fixed $Fe_{0.9}Ni_{0.1}$ ratio with variable S, P and C, and homogenised in an agate mortar under ethanol for at least 1 hour. Starting mixes were dried and then stored for a minimum of 12 hours in a vacuum oven at 120 °C prior to use.

Experimental methodology

High-pressure experiments were performed using an end-loaded piston-cylinder apparatus at the University of Edinburgh. For experiments at 0.5 GPa, starting mixes were loaded into 4mm o.d., 2mm i.d., 5mm long graphite or MgO capsules with integral stepped lids, machined from crushable rods. Experiments at 1.0 GPa were conducted using either one or two (2.5 mm length) hBN capsules. Capsules were stored overnight in vacuum ovens prior to use, and loaded capsules stored in a drying oven for several hours after loading. Prior to, and after machining, hBN capsules were stored in a vacuum oven. Similarly, ceramic (Al_2O_3) internal components in high-pressure assemblies were also stored in a drying oven prior to use.

Capsules were loaded into high temperature 0.5” talc-pyrex-graphite piston cylinder assemblies (Potts *et al.*, 2021), surrounded by fired Al_2O_3 ceramic spacers. In accordance with previous studies (Corgne *et al.*, 2008; Dasgupta *et al.*, 2009) short run durations of 0.5-4 hr were used (1) because of rapid chemical equilibrium in superliquidus Fe-rich systems, even between samples and surrounding capsules, (2) to minimise any ingress of metallic liquids into surrounding capsules, including percolation but also more rapid melt injection during melting (Berg *et al.*, 2018), and

to minimise H ingress into sample volumes. All experiments were pressurised at room temperature before heating at 100 °C/min to 800 °C. Most experiments were held at 800°C for approx. 12 hours to anneal polycrystalline capsules, which Grewal and Asimow (2023) noted is required to minimise sample volatile loss and melt migration at higher temperatures. However, we note here that annealing at 800°C did not prevent volatile loss in 0.5 GPa experiments, which was only minimised by annealing at the final run temperature. A small number of experiments were not annealed to determine the effect of annealing on volatile loss and textural development. From 800°C, all samples were heated at approximately 150°C/min to the final run temperature of 1400 °C. Temperatures were monitored using internal Pt-Pt13%Rh thermocouples, shielded from samples by a 1mm thick sintered Al_2O_3 disc. No metallic melt ingress into discs was observed, and consistent power-temperature relationships were observed across experiments. Run pressure and temperature were continually monitored and maintained before rapid isobaric quenching by turning off power to the heating circuit.

Recovered samples were mounted in CrystalBond™ and ground with 1200 grit SiC grinding paper to reveal longitudinal sections, before being polished with 0.3 µm colloidal Al_2O_3 suspension on a polishing mat. Polished samples were removed from mounts by soaking in high-purity acetone, and remounted in indium within 1" aluminium sample holders, for analysis. Prepared samples were stored under vacuum at room temperature in a desiccator. Experiments conducted using graphite capsules were mounted separately from other samples to avoid contamination.

Sample characterisation and analysis

Samples were studied optically and using a Carl Zeiss SIGMA HD VP Field Emission Scanning Electron Microscope (SEM) with a dual Energy Dispersive Spectrometer (EDS) system and Oxford AZtec software for X-ray compositional analysis. Prior to analysis, sample surfaces were plasma cleaned (2x 60 s bursts) under vacuum and coated with an approximately 2.5 nm layer of Al. Samples were characterised and analysed using a 20kV accelerating voltage, 70 µm aperture, and at a fixed 7.0 mm working distance. Here, we use SEM-EDS to determine compositions of run products as, despite having lower energy resolution in X-ray spectra compared to wavelength dispersive spectrometry used in electron microprobe analysis, it conveys several advantages: (1) EDS-SEM analysis is rapid, with energy range profiles obtained here in <15s, thus minimising issues with volatile loss from, and frequently noted carbon deposition onto, sample surfaces during analysis; (2) any systematic changes in X-ray intensities during prolonged analysis can more easily time-resolved and determined; (3) compositional data can be obtained by rastering the primary beam over selected areas, which greatly facilitates analysis of texturally complex samples produced by exsolution of Fe/Ni and S-bearing liquids during quenching. This is a particular advantage here due to coarse exsolution textures in some samples which prohibited analysis by EMPA (Fig. S-1).

An Al-coated Co standard was used to calibrate EDS spectra. To more accurately determine C contents in run products, samples were mounted with the following secondary standards: Fe_3C (6.67 wt. % C, synthesised from homogenised high purity Fe and diamond powders at 2 GPa/1200 °C for 72h in a piston-cylinder apparatus, within a MgO capsule, as described in Dasgupta and Walker (2008), and verified by X-ray diffraction), carbon steel standards ECRM 090-1(C) (1 wt. % C) and ECRM 084-1(C) (0.4 wt. % C), and to characterise the C background, a C-free (C blank) high-purity Fe standard (ECRM097-2). To minimise drift in the calibration during analytical sessions, the e^- beam was left to stabilise for 1 hour prior to data collection. EDS data were calibrated at the start of sessions using the Co and C standards, and recalibrated throughout analytical sessions, typically every 1.5 hours. C analysis using electron beam techniques is challenging due to high backgrounds and problems with C deposition onto samples during analysis (e.g., Dasgupta *et al.*, 2009; Grewal *et al.*, 2019a,b). During calibration and recalibration, the C-free standard (C blank) was used to assess the C background on measurements. A time-variable C background, typically 0.5 wt. %, was applied. Repeat analyses

across different sessions was also used to ensure consistency. Sample coatings were removed and samples cleaned and recoated between analytical sessions.

Results from super-liquidus experiments

Textures in recovered samples

Fig. S-1 shows examples of textures noted in run products. Experimental details are listed in Table S-1 and compositions of run products listed in Table S-2. All runs consist of a (quenched) single miscible liquid or coexisting immiscible Fe-rich and FeS-rich liquids. Some C-rich experiments in MgO and BN capsules also contained graphite, implying C saturation in run products. Samples in graphite capsules are also assumed to be C-saturated, although we noted no clear evidence of graphite crystallisation within sample volumes. Detailed discussion of textures in run products is given below.

An initial series of experiments was conducted at 0.5 GPa using graphite and MgO capsules. All experiments using graphite capsules resulted in immiscibility, and extensive segregation of Fe-rich and FeS-rich liquids within capsules (Fig. S-1A). However, the presence of small regions of quenched FeS-rich liquid in larger regions of Fe-rich liquid, and vice versa (Fig. S-1A), demonstrates that segregation did not go to completion. Fe-rich liquids, and especially FeS-rich liquids, in graphite capsules have coarse exsolution textures formed during quenching (quench times estimated to be 1400-1000 °C in approx. 5 s, and 1400-300 °C in approx. 15 s). These textures create challenges with polishing and analysis, especially accurate determination of C contents due to pitted surfaces. As reliable C contents of run products in graphite capsules could not be determined they are not reported here.

Exsolution textures in quenched FeS-rich liquids are slightly finer in experiments using MgO capsules, and vary significantly depending on bulk composition and phase stability. Finer exsolution textures are noted in experiments in which a single miscible liquid is present (e.g., Fig. S-1B). Coarser exsolution textures are apparent in run products with immiscible liquids, especially in quenched FeS-rich liquids (Fig. S-1C). Reactions rims a few 10s µm in diameter between run products and MgO capsules were observed in all experiments (Fig. S-1D), implying the exchange $(x+1)Fe_{Fe\ liquid} + (1-x)MgO_{capsule} + (1+x)/2O_2 = FeO_{Fe\ liquid} + (Fe_xMg_{1-x})O_{capsule}$. In some run products, an additional P-rich region was noted, apparent as a small reaction rim of multi-phase crystalline material adjacent to (Fe,Mg)O rims and consisting of Mg, Fe, O and P, but on the opposite side of these rims to the sample volume (Fig S-1D). Presence of P in these regions implies P loss from run products (as discussed below) and reaction with surrounding capsules, prior to Fe-MgO exchange. Only very minor melt percolation into MgO capsules was noted.

To minimise P and S loss from run products, a second series of experiments were performed at 1 GPa. These experiments additionally used hBN capsules to minimise sample/capsule exchange. Differences in MgO and BN thermal conductivity explain differences in textures of recovered run products, with exsolution textures in all quenched liquids in hBN capsules being finer (Fig. S-1, F-H). Phase separation in these experiments, in contrast, is less developed than in corresponding experiments performed in MgO capsules, despite longer run durations. The reason for textural differences is unclear, but might result from small differences in bulk composition, with experiments in graphite capsules being C-saturated, and experiments in both graphite and h-BN capsules producing run products with slightly lower O contents.

Composition of run products

Due to variably coarse exsolution textures in many samples, SEM-EDS data were collected from defined regions of samples to determine representative phase compositions (20x20µm to >100x100µm). Initial analysis of run products

revealed no systematic variations in compositions across sample volumes, e.g., from centres to edges of samples, which might occur in 0.5 GPa samples if volatile loss had occurred progressively during experiments. Regardless, to minimise any effect of volatile loss, or any influence of sample/capsule interaction, compositional data reported here are from central regions of samples, and were collected during a limited number of later analytical sessions to minimise variations in C backgrounds. For samples with immiscible liquids, compositions were determined for adjacent coexisting regions of each phase, to further minimise any effect of small variations in liquid composition. Compositional data reported in Table S-2 are averages of all regions analysed and are not weighted for the area of regions analysed. Standard deviations are internal variation in phase compositions across multiple area analyses. Due to low concentrations present, errors for determined O and C contents, and in some cases P, are likely to be higher. Actual errors on reported C contents also include variations in the C background, which was typically ~0.5±0.1 wt. %. No detectable C was found in samples which were nominally C-free. Given C backgrounds of ~0.5 wt. %, detection limit for C is estimated to be 0.2-0.3 wt. %. Although C was not detected in experiments performed using nominally C-free starting mixes, use of graphite furnaces in piston-cylinder assemblies likely resulted in minor C ingress into run products.

EDS analysis did not reveal the presence of other elements. Grewal and Asimow (2023) demonstrated N solubilities in Fe-rich liquids of around 0.5 wt. % under comparable conditions. Use of hBN capsules presumably results in incorporation of minor N into experimental products, although this was not detected here. We estimate that the detection limit for N by EDS spectrometry is likely around 0.1 wt. %. As such, N content of run products here is considerably lower than noted in Grewal and Asimow (2023), although that study utilised starting mixes which were N-bearing.

Fe:Ni ratios are constant in run products, with immiscible liquids having Fe:Ni ratios of approximately 0.9, i.e. identical to bulk compositions. Therefore, although Ni has a significant effect in mixing properties of Fe-rich liquids and, for example, C solubility (Zhang *et al.*, 2018), Ni is not selectively partitioned between FeS-rich and Fe-rich liquids.

Experiments at 0.5 GPa experienced variable volatile loss, most evident in run products with a single miscible liquid. C loss (not including C-free experiments or those with coexisting graphite) varied from 0-8 wt. % (4 wt. % average), P loss varied from 35-85 wt. % (65 wt. % average) and S loss from 0-90 wt. % (30 wt. % average). Losses are based on comparison to ideal starting compositions which were not verified, and errors on these estimates are likely higher for C and P due to low concentrations present. There are no discernible correlations of % loss with bulk composition or run duration. Volatile loss in experiments with immiscible phases is harder to determine but appears to be similar in extent. Loss of P is consistent with the presence of minor P in MgO capsules, although no comparable S-bearing phases were noted. Volatile loss from Fe-alloys is commonly noted in experimental studies, and can be minimised by annealing experiments during heating (e.g., Grewal and Asimow, 2023). Here we noted that annealing at 800 °C for around 12h had no consistent effect in reducing the extent of volatile loss in 0.5 GPa experiments. Similarly, extent of volatile loss appeared independent of duration at final run temperature (1400 °C) and bulk composition. Comparable volatile loss in graphite and MgO capsule experiments, absence of any clear compositional zonation across samples, such as systematic reduction in volatile contents towards the edge of samples, the presence of P-rich and Fe-rich rims in MgO capsules adjacent to samples, and a lack of any clear correlation between volatile loss and experimental duration (in addition to compositional data as discussed below) all suggest that (1) volatile loss is driven by volatility, with P loss > S loss > C loss, and (2) volatile loss likely occurred early in experiments and/or during heating. Rapid capsule recrystallisation at high temperature likely minimised volatile loss. Experiments performed at 1.0 GPa record only minor volatile loss, suggesting the loss at lower pressure is due to inherent volatility of P, S and to a lesser degree C. This is consistent with only minor volatile loss in other experimental studies conducted at higher pressure (e.g., Dasgupta and Walker, 2008; Zhang *et al.*, 2018). We note that liquid compositions and phase relations are consistent between 0.5 and 1.0 GPa experiments, further indicating that volatile loss occurred during the initial stages of 0.5 GPa experiments, and that

equilibrium was then rapidly attained, and bulk compositions remained constant, during the latter stages of experiments, i.e. once final run temperature had been attained.

Previous experiments on high pressure Fe-alloy liquids have noted the presence of minor O in run products, including those performed using MgO (Grewal and Asimow, 2023; Dasgupta *et al.*, 2009) and graphite capsules (Corgne *et al.*, 2008; Dasgupta *et al.*, 2009; Zhang *et al.*, 2018). For MgO capsule experiments, O incorporation is likely due to capsule-sample exchange, and O contents here for miscible liquids are comparable to previous studies. In accordance with those studies (Corgne *et al.*, 2008; Dasgupta *et al.*, 2009), we note that O partitions into FeS-rich liquids. Overall, O contents are higher in experiments performed in MgO capsules, probably as a result of slightly higher oxygen fugacity, although O is present in experiments performed in graphite and hBN capsules. Oxygen fugacity here, similar to previous studies (Corgne *et al.*, 2008; Grewal and Asimow, 2023), is expected to range from c. log fO_2 = iron-wüstite (IW) to IW-2, comparable to estimates of fO_2 during differentiation in parent bodies to magmatic iron meteorites (Grewal *et al.*, 2024).

Modelling planetesimal core compositions

Modelling based on chondrite data

Iron meteorites, or more specifically the parental liquids from which iron meteorites formed (termed here "iron meteorite parental liquids, IMPLs), are believed to represent the cores of differentiated planetesimals which originally had chondritic compositions (e.g., Goldstein et al., 2009). Comparison of IMPLs and average chondritic compositions can, therefore, be instructive. Chondrite compositional data (e.g., Fig. 3) clearly demonstrate significant variations in volatile element content. Petrological type for chondrites represents the degree of aqueous alternation (1-2) and thermal metamorphism (4-6) (Goldstein et al., 2009); the latter provides a proxy of peak temperature attained, and has been used to assess the extent of volatile element loss in parent bodies due to processes such as degassing (e.g., Hirschmann *et al.*, 2021). During planetesimal differentiation at higher temperatures than attained by primitive meteorites, additional volatile loss would be expected. As such, IMPLs likely record additional volatile-loss in planetesimals that is not recorded by chondritic meteorites. Conversely, the compositions of IMPLs may have been affected by processes which occurred after core-formation, such as planetesimal disruption, progressive cooling and degassing, and later impact events (e.g., Yang *et al.*, 2007, 2010).

Here, in order to compare compositions of IMPLs with average chondritic compositions, we model differentiation in chondritic-composition planetesimals by assuming metal/silicate segregation after the method of Bercovici *et al.* (2022). First, we assembled average initial compositions of the same set of chondrite groups, namely H, L, LL, CO, CI, CM, CV, CK. As Bercovici *et al.* (2022) do not record full compositions used in their modelling, we used data from Jarosewich (2006) to obtain a bulk composition of each meteorite class. Sub-lithology compositions quoted in the data were ignored, and for paired meteorites or meteorites with multiple measurements we took a simple average of the compositions (Table S-3). From Figure 3 it is clear that there is substantial variation in the C content within chondrite groups. Hirschmann *et al.* (2021) argued that systematic trends in log C/S versus log C record degassing and both C and, to a lesser extent, S loss from chondrite parent bodies. However, here we argue here that variation in C is independent of S for petrological types 3-6, and more likely records nebular processes (inherent variation in volatile content) and lower temperature degassing (loss of C), i.e. distinct from high temperature degassing related to petrological type. As experiments demonstrate an important role for C in driving immiscibility in Fe-rich liquids, and as C contents in chondrites are variable and record lower-temperature degassing, we used two approaches to assess ranges of C content of model 'chondrite' planetesimal cores. Firstly, we used average concentrations from Jarosewich (2006) for petrological types 3-6 (Table S-3), i.e. those not affected substantially by aqueous alteration, to determine core S, P and C contents. We then additionally used the full range of C compositions given in the MetBase meteoritical database

(Hezel, 2020) for petrological types 3-6 (i.e. variability shown in Fig. 3) to determine minimum C contents for each average chondrite composition. We used the same modelling approach to determine core compositions based on these 'minimum C' chondrite compositions.

For modelling 'chondrite' core compositions, we partitioned elements in initial chondrite compositions into either 'core' or 'mantle'. Of the compositional elements recorded in the Jarosewich (2006) tables, we partitioned FeO, SiO_2, Al_2O_3, MgO, Na_2O, CaO, K_2O, TiO_2 and MnO into the mantle, and Fe(metal), Ni(metal), Fe from FeS, NiO, Ni from NiS, P from P_2O_5, C, and C from CO_2 into the core. S was partitioned between core and mantle after Bercovici *et al.* (2022). However, in contrast to Bercovici *et al.* (2022), we assign C and P to the core entirely. This is a reasonable assumption for siderophile C, except under more reducing conditions than considered here (log fO_2 = IW-3 or lower, i.e. 3 log units below the Fe-FeO buffer) where graphite is stabilised (Keppler and Golabek, 2019). In contrast, phosphorous is moderately siderophile (Gu *et al.*, 2019), so would be partially retained in the silicate portion of a differentiating planetesimal, depending on factors such as oxygen fugacity and extent of silicate melting. As the solubility of P in Fe-rich melts is dependent on S content, silicate/metal P partitioning might depend on the S content of core-forming liquids. Conversely, textural and compositional evidence from high temperature partial melting experiments in chondritic systems demonstrates that (1) P-rich phases break down at relatively low temperatures, implying that P partitioning can be considered in terms of metal/silicate melt partitioning, and (2) S-rich core-forming liquids incorporate significant P up to at least moderate degrees of silicate melting (Bromiley, 2023). Therefore, based on metal/silicate melt partition coefficients from Gu *et al.* (2019) ($D_{metal/silicate}$ ~7-12, by weight), we assume that all P partitions into our modelled cores. Regardless, as a consequence of the assumption that P and C partition into core-forming liquids, our approach places upper bounds on the amounts of these elements in planetesimal cores. As P is a minor element in planetesimal compositions (averaged chondrite compositions contain up to 0.26±0.04 wt. % P_2O_5), the effect of assuming that P partitions entirely into differentiated cores is probably quite minor. Standard deviations for each element in averaged compositions were propagated through our models, and are reported as uncertainties in core compositions in Table S-4.

Modelled 'chondrite core' compositions are shown in Figure 2B and S-2B. Solid red circles are core compositions based on average chondrite compositions. Open red circles are compositions based on minimum C contents. Uncertainties in S and P result from large standard deviations in both for averaged compositions, i.e. they reflect large variations in S and P content within each chondrite group, in part as a result of volatile loss. Comparison of 'average' and 'minimum' C contents in Figure 2B indicates of how variability in C contents of chondrites results in variable estimated C contents in cores, due to low-temperatures degassing but also due to variability in chondrite compositions. Similar, but not identical to Bercovici *et al.* (2022), we find H chondrites are expected to produce the lowest S concentration in the core (9 ± 8 wt. %) and CI have the highest (37 wt. %). As noted by Bercovici *et al.* (2022), high S contents in modelled core compositions, in addition to other light elements, implies liquid immiscibility and presence of coexisting Fe-rich and FeS-rich liquids (Fig. S-2B) independent of C content. C contents based on average chondrite compositions vary from 0.75 ± 0.09 wt. % for CK chondrites to 18.23 wt. % for CV chondrites. For most carbonaceous chondrite groups, C contents of model cores are unrealistically high, and exceed C saturation (Zhang *et al.*, 2018). This is not unsurprising, as significant low temperature degassing and loss of C is expected during planetesimal heating. If it is assumed that C loss is largely a low-temperature processes, and recorded by the large variability in C contents across all chondrite data (Fig. 3), minimum C content of chondrites provide a more realistic estimation of the C content of planetesimal cores. Corresponding 'minimum' core C contents range from 0.07 ± 0.01 wt. % for CI chondrites to 3.30 ± 1.45 wt. %, but with most values <1 wt. %. Based on minimum compositions, C, S and P contents of modelled cores imply that all except that based on the L chondrite would be immiscible liquids.

Iron-meteorite parental liquid compositions

In comparison to IMPLs, planetesimal cores modelled from minimum C chondritic compositions are light element-rich. IMPLs contain, on average, 1-15% of the C present in these model chondritic cores, around 50% of the S, and around 75% of the P. As such, IMPL compositions record variable volatile loss/depletion compared to chondritic compositions, with significant differences in C content, and small to moderate differences in S and P content. Comparison may provide insight into light element loss during differentiation of IMPL planetesimals. S-, P- and C-loss from our 0.5 GPa experiments provides a useful context to this discussion. In these experiments, volatile loss from Fe-rich samples occurred during heating, and was only inhibited once run temperatures were reached and, presumably, following rapid grain growth in both MgO and graphite capsules. Experiments record greatest loss of P, followed by S, and minor to no loss of C, although we caution that there are significantly greater analytical errors for low C and P contents in most samples. Regardless, it appears unlikely based on these observations that the volatile-poor nature of IMPL compared to chondritic compositions can be explained entirely by volatile loss from liquid iron (i.e. from unshielded planetesimal cores after disruption), which would result in the opposite trend of P loss > S loss > C loss. Bercovici *et al.* (2022) suggested that immiscibility and separation of S-rich liquid (i.e. FeS-rich liquid) might explain the variably S-poor nature of IMPLs, assuming that these form via crystallisation of the corresponding Fe-rich liquid. Our data suggest that liquid segregation would result in Fe-rich liquids which were S-depleted, but significantly P- and C-enriched relative to model chondritic cores, inconsistent with IMPL compositions. Hirschmann (2021) noted that extensive C loss, and minor S loss is more likely to be a signature of magma ocean degassing from differentiating planetesimals. It is possible, therefore, that volatile contents of IMPLs reflect multiple degassing processes, including (1) low temperature degassing and loss of C (evidenced by trends in log C/S versus log C); (2) volatile loss during higher temperature metamorphism, and eventually partial melting, in planetesimals (Hirschmann *et al.*, 2021); and (3) variable volatile loss during planetesimal disruption and/or during later cooling of unshielded or partially-shieled cores (e.g., Yang *et al.*, 2007, 2010; Matthes *et al.*, 2018; Hunt *et al.*, 2022; Grewal and Asimow, 2023;). Comparison of chondritic and iron meteorite compositions highlights two important devolatisation processes: extensive loss of C at lower temperatures, and, higher temperature loss of P, S and C.

The extent of volatile loss during core-formation, i.e. at temperatures exceeding those to which chondritic material was subjected, will depend on the thermal history of planetesimals and the extent of silicate melting. Several thermochemical models suggest that sustaining substantial magma oceans on planetesimals is difficult. Instead, planetesimal differentiation may have only proceeded following localised, short-lived melting of silicate (e.g., Kaminski *et al*., 2020), or within internal magma oceans overlain by thick, chondritic shells, which would have reduced the extent of degassing (e.g., Lichtenberg *et al.*, 2019; Sturtz *et al.* 2022). The extent to which segregation of core-forming liquids could proceed via percolation through solid silicate, or with only limited silicate melting, is also unresolved (Bromiley, 2023). IMPLs represent a population of volatile-poor planetesimal core compositions, variably modified post-differentiation. Likewise, model chondrite core compositions are volatile-rich, as chondrite compositions do not record volatile loss during differentiation. We argue that both approaches bracket planetesimal core compositions, and that core composition and the extent of immiscibility would depend on the thermal history of planetesimals, which was likely variable. Large-scale planetesimal melting would result in extensive volatile loss and formation of volatile-poor (miscible) cores. In contrast, planetesimals which experienced minor or localised silicate melting during differentiation would form volatile-rich cores. As chondrites experienced peak thermal metamorphism extending up to the eutectic temperature of Fe,Ni-FeS, at least for some groups of ordinary chondrites (e.g., H, L, LL, Mare *et al.*, 2014), modelled chondrite compositions (Fig. 2B, Fig S-2B) indicate that volatile-rich planetesimal cores may have consisted of immiscible Fe-rich and FeS-rich liquids. As noted in the main text, one example of minor degassing during differentiation may be icy moons in the outer solar system which have metallic cores. It has been suggested that some icy/rocky moons have carbonaceous chondrite bulk compositions, and formed by slow heating and differentiation over 100 Myr timescales (e.g., Melwani Daswani *et al.*, 2021; Trinh *et al.*, 2023). Low-temperature core-formation in these bodies, i.e. without silicate melting,

would result in the formation of FeS-rich cores if segregation could proceed at temperatures of the Fe,Ni-FeS eutectic, or layered Fe-rich inner/FeS-rich outer cores.

Modelling core solidification

We modelled progressive crystallisation of core-forming liquids based on incremental removal of small batches of crystalline Fe,Ni, using experimentally-based partition coefficients. Calculations were performed for three compositions which lie within the 1 liquid field in Figure 1: 8 wt. % S, 1 wt. % P, 0.2 wt. % C; 19 wt. % S, 0.1 wt. % P, 0.1 wt. % C; 12 wt. % S, 1 wt. % P, 0.001 wt. % C. In each model increment we assumed 1 % crystallisation (by weight), and calculated remaining liquid composition. We used fixed Fe and Ni solid/liquid coefficients from experiments of Grewal and Asimow (2023), based on their data at 1350°C in the S-rich system (8 wt. % S), which most closely matches liquid compositions modelled here. We assumed negligible S incorporation into solid Fe,Ni. In contrast, P and C can be incorporated into both solid and liquid phases. Due to the non-ideal nature of Fe-rich liquids, partition coefficients for both are expected to vary significantly with liquid composition, especially S content. We use the compositional dependence of P solid/liquid partitioning from Zhai *et al.*, (2022), derived from experiments in a C-free system. There is limited data on solid/liquid C partitioning. Grewal and Asimow (2023) noted that their experimental dataset is not comprehensive enough to separate the coupled effects of liquid S content and temperature on C partitioning, although suggested that S content has a significantly greater influence. For internal consistency, we fit their experimental data in the 8 wt. % S bulk composition (5 data points) to an empirical function to interpolate compositional dependence of C partitioning of the form:

$$D_C^{solid/liquid} = A + B\left(1 + e^{-\frac{C_S - C}{D}}\right)$$

where $D_C^{solid/liquid}$ is the C partition coefficient (by weight) C_s is weight % S in liquid. A to D are constants which we determined by least squares fitting (A =0.67, B=2.31, C=24.6 and D=2.04; ssr=2.4×10^{-4}). This assumes no effect of temperature on C partitioning. In our models, therefore, we simulated continued extraction of 1% solid Fe,Ni, normalising remaining liquid compositions to 100% after each step. Calculations were stopped once liquid composition approached c. 30 wt. % liquid.

Although there are large uncertainties in partition coefficients used, and results are dependent on the batch equilibrium crystallisation model used, clear compositional controls on element partitioning arising from non-ideal mixing in Fe-rich liquids mean that general trends in liquid composition are likely correct. Solidification of core-forming liquids results in an increase in liquid S content, which eventually results in a marked increase in compatibility of P and C into the solid phase. Therefore, liquid P- and C- contents can increase during initial stages of solidification, but then rapidly decrease one a threshold liquid S content is reached, which will vary depending on partition models used. For C-poor compositions, especially IMPL compositions, this means that liquids can remain in the 1-liquid field. Other compositions can enter the 2-liquid stability field.

Supplementary Tables

Table S-1 Starting materials (in addition to $Fe_{0.9}Ni_{0.1}$), experimental conditions and run products. All experiments are superliquidus (in terms of Fe alloys) with run products consisting of a single alloy/miscible liquid (M-L), or immiscible Fe-rich liquid (C-rich, P-rich, S-poor, or 'Fe-L') and FeS-rich liquid (C-poor, P-poor, S-rich, or 'FeS-L'), ± graphite (gr). Experiments performed in graphite capsules, and where graphite formed in run products are considered C saturated (C sat). [1]Phase proportions (as %) estimated for immiscible liquids based visual observation of run products from central sections of recovered samples.

Exp.	Starting mix (wt. %)			Capsule	Pressure (GPa)	Anneal at 800 °C?	Duration at 1400 °C	Run products[1]	C sat?
	S	P	C						
IM_6	5	3	0	Gr.	0.5	Yes	30	Fe-L (95) + FeS-L (5)	Yes
IM_7	15	3	0	Gr.	0.5	Yes	30	Fe-L (55) + FeS-L (45)	Yes
IM_8	5	3	0	MgO	0.5	No	45	M-L	No
IM_9	5	1.5	0	Gr.	0.5.	No	30	Fe-L (3) + FeS-L (97)	Yes
IM_10	15	1.5	0	Gr.	0.5	Yes	30	Fe-L (45) + FeS-L (55)	Yes
IM_12	5	3	1	MgO	0.5	Yes	60	M-L	No
IM_13	5	3	3	MgO	0.5	Yes	60	M-L	No
IM_14	5	3	0.5	MgO	0.5	Yes	60	M-L	No
IM_15	5	3	5	MgO	0.5	Yes	60	M-L + gr	Yes
IM_17	15	1.5	0	MgO	0.5	Yes	40	M-L	No
IM_19	15	1.5	1	MgO	0.5	Yes	65	Fe-L (60) + FeS-L (40)	No
IM_20	10	1	0	MgO	0.5	Yes	60	M-L	No
IM_21	10	1	1	MgO	0.5	No	90	M-L	No
IM_22	10	1	1	MgO	0.5	Yes	80	Fe-L (65) + FeS-L (35)	No
IM_23	5	3	5	MgO	0.5	Yes	90	M-L + gr	Yes
IM_24A	15	1.5	0	BN	0.5	Yes	35	M-L	No
IM_24B	15	1.5	1	BN	1.0	Yes	35	Fe-L (50) + FeS-L (50)	No
IM_25	10	1	1	BN	1.0	Yes	250	Fe-L (80) + FeS-L (20)	No
IM_26B	15	3	0	BN	1.0	Yes	330	Fe-L (55) + FeS-L (45)	No
IM_27A	10	1	0	BN	1.0	Yes	300	M-L	No
IM_27B	5	3	3	BN	1.0	Yes	300	Fe-L (85) + FeS-L (15)	No
IM_28A	5	3	1	BN	1.0	Yes	120	M-L	No
IM_28B	15	0.5	1	BN	1.0	Yes	120	Fe-L (50) + FeS-L (50)	No

Table S-2 Averaged compositions of run products. na= not analysed; bdl = below detection limit.

Exp.	C		O		P		S		Fe		Ni	
	wt. %	σ	wt. %	σ	wt. %	σ	wt. %	σ	wt. %	σ	wt. %	σ
Miscible (single) liquid (M-L)												
IM_8	bdl		bdl		1.9	0.2	3.7	0.4	84.4	0.4	9.9	0.1
IM_12	1.1	0.4	0.8	0.1	0.9	0.1	3.0	0.2	83.0	0.5	11.2	0.2
IM_13	3.2	0.7	0.8	0.1	0.6	0.0	3.2	1.0	82.5	1.1	9.8	0.2
IM_14	0.5	0.3	1.0	0.1	1.6	0.1	3.3	0.2	84.0	0.2	9.5	0.2
IM_15	3.4	0.6	0.8	0.2	0.9	0.0	3.6	0.9	82.7	1.3	8.6	0.2
IM_17	bdl		1.9	0.2	0.4	0.1	14.8	0.6	73.8	0.5	9.1	0.2
IM_20	bdl		1.2	0.3	0.4	0.1	11.0	0.2	78.1	0.5	9.3	0.1
IM_21	1.0	0.2	1.0	0.1	0.1	0.0	6.1	0.7	77.9	0.8	13.7	0.2
IM_23	3.7	0.6	0.8	0.1	0.8	0.1	2.4	0.4	83.0	0.5	9.4	0.2
IM_24A	bdl		1.2	0.1	1.3	0.1	15.1	0.4	74.0	0.4	8.4	0.2
IM_27A	bdl		1.1	0.1	1.5	0.1	9.6	0.2	79.3	0.3	8.5	0.2
IM_28A	1.1	0.5	0.8	0.1	2.8	0.1	4.3	0.2	80.8	0.6	10.2	0.3
FeS-rich immiscible liquid (FeS-L)												
IM_6	na		1.6	0.4	0.1	0.1	27.8	2.2	62.4	0.1	8.0	2.1
IM_7	na		1.9	0.3	0.2	0.2	28.0	0.5	61.9	0.9	8.1	0.4
IM_9	na		2.0	0.2	0.1	0.2	28.1	0.6	59.2	0.8	10.6	1.1
IM_10	na		4.2	1.2	0.1	0.1	26.7	1.0	62.0	1.1	7.1	1.6
IM_19	0.4	0.5	3.8	0.4	0.0	0.0	26.3	1.3	61.5	2.0	8.1	2.6
IM_22	0.1	0.1	2.8	0.5	0.0	0.0	30.3	1.3	55.5	1.9	11.4	1.4
IM_24B	0.8	0.2	1.1	0.1	0.2	0.0	25.6	0.4	62.9	0.5	9.3	0.5
IM_25	0.4	0.4	1.7	0.2	0.2	0.0	23.9	1.1	64.5	0.9	9.4	0.6
IM_26B	bdl		1.4	0.5	0.2	0.0	26.9	0.3	63.2	0.4	8.3	0.5
IM_27B	0.5	0.4	1.0	0.1	0.2	0.0	27.5	0.5	61.3	0.2	9.5	0.4
IM_28B	0.6	0.1	1.6	0.1	0.0	0.0	24.2	0.2	64.8	0.3	8.8	0.2
Fe-rich immiscible liquid (Fe-L)												
IM_6	na		0.2	0.3	2.2	0.1	1.1	0.1	87.1	0.6	9.4	0.2
IM_7	na		bdl		3.6	0.5	1.3	0.3	83.9	1.3	11.2	0.9
IM_9	na		bdl		0.8	0.1	1.6	0.2	87.1	0.3	10.6	0.1
IM_10	na		bdl		1.4	0.1	1.6	0.2	86.3	0.2	10.7	0.2
IM_19	2.0	0.8	1.0	0.0	0.1	0.1	2.2	0.6	83.3	0.7	11.5	0.3
IM_22	2.1	0.7	1.0	0.1	0.0	0.0	2.2	0.6	80.0	0.7	14.5	0.7
IM_24B	1.4	0.4	0.9	0.1	2.3	0.0	2.5	0.1	82.9	0.3	9.9	0.2
IM_25	1.3	0.8	0.9	0.2	0.9	0.3	3.7	0.7	83.0	1.1	9.8	0.4
IM_26B	bdl		0.7	0.1	4.3	0.2	1.3	0.4	82.3	1.2	11.3	1.7
IM_27B	3.8	0.8	1.0	0.5	3.5	0.3	1.7	0.4	81.5	0.9	8.5	0.5
IM_28B	2.4	0.7	0.7	0.1	0.9	0.1	2.1	0.1	86.3	0.6	7.6	0.2
Immiscible liquid bulk composition[1]												
IM_6	na		0.2	0.0	2.1	0.3	2.5	0.4	85.9	12.9	9.4	1.4
IM_7	na		0.8	0.1	2.1	0.3	13.3	2.0	74.0	11.1	9.8	1.5
IM_9	na		0.1	0.0	0.8	0.1	2.4	0.4	86.2	12.9	10.6	1.6
IM_10	na		2.3	0.3	0.6	0.1	15.4	2.3	72.9	10.9	8.7	1.3

Exp.	C		O		P		S		Fe		Ni	
	wt. %	σ	wt. %	σ	wt. %	σ	wt. %	σ	wt. %	σ	wt. %	σ
IM_19	1.3	0.2	2.1	0.3	0.0	0.0	11.9	1.8	74.6	11.2	10.1	1.5
IM_22	1.4	0.2	1.6	0.2	0.0	0.0	12.0	1.8	71.4	10.7	13.4	2.0
IM_24B	1.1	0.2	1.0	0.1	1.3	0.2	14.0	2.1	72.9	10.9	9.6	1.4
IM_25	1.2	0.2	1.1	0.2	0.8	0.1	7.7	1.2	79.3	11.9	9.7	1.5
IM_26B	0.0	0.0	1.0	0.2	2.5	0.4	12.8	1.9	73.7	11.1	10.0	1.5
IM_27B	3.3	0.5	1.0	0.1	3.0	0.4	5.5	0.8	78.5	11.8	8.7	1.3
IM_28B	1.5	0.2	1.1	0.2	0.4	0.1	13.1	2.0	75.6	11.3	8.2	1.2

[1]based on estimated proportions of FeS-rich and Fe-rich liquids

Table S-2 continued

Table S-3 Calculated averaged chondrite compositions (wt. %) based on compositions reported in Jarosewich (2006)

Species	H	L	LL	CO	CV	CK	CM	CL
SiO_2	36.34	39.62	40.75	33.16	34.15	34.36	29.45	22.69
SiO_2 σ	1.05	0.61	0.65	1.36	0.26	0.23	1.51	nd
TiO2	0.12	0.13	0.13	0.13	0.17	0.16	0.12	0.07
TiO2 σ	0.01	0.01	0.02	0.01	0.01	0.03	0.01	nd
Al2O3	2.13	2.27	2.25	2.81	3.25	3.01	2.35	1.70
Al2O3 σ	0.14	0.14	0.12	0.27	0.10	0.23	0.21	nd
Cr2O3	0.51	0.52	0.54	0.48	0.51	0.51	0.45	0.32
Cr2O3 σ	0.04	0.04	0.03	0.02	0.04	0.01	0.05	nd
FeO	10.28	14.70	17.41	24.26	23.33	28.18	21.50	16.82
FeO σ	2.01	1.59	1.94	4.26	4.58	0.67	0.85	nd
MnO	0.31	0.33	0.34	0.23	0.18	0.18	0.23	0.21
MnO σ	0.02	0.02	0.02	0.04	0.02	0.01	0.03	nd
MgO	23.03	24.65	25.19	22.48	24.34	25.06	20.14	15.87
MgO σ	0.74	0.49	0.52	1.75	0.58	0.14	1.33	nd
CaO	1.72	1.85	1.95	1.94	2.48	2.53	1.86	1.36
CaO σ	0.10	0.10	0.11	0.35	0.30	0.12	0.11	nd
Na2O	0.79	0.92	0.94	0.45	0.32	0.45	0.53	0.76
Na2O σ	0.14	0.11	0.07	0.31	0.21	0.05	0.15	nd
K2O	0.09	0.10	0.10	0.05	0.04	0.03	0.05	0.06
K2O σ	0.02	0.02	0.02	0.02	0.02	0.01	0.01	nd
P2O5	0.26	0.23	0.23	0.22	0.25	0.23	0.24	0.22
P2O5 σ	0.04	0.04	0.06	0.02	0.05	0.01	0.04	nd
H2O+	0.85	0.52	0.53	2.25	0.78	0.40	7.85	10.80
H2O+ σ	0.95	0.58	0.51	2.06	0.87	0.14	3.64	nd
H2O-	0.26	0.15	0.21	1.03	0.75	0.33	1.82	6.10
H2O- σ	0.24	0.15	0.13	0.82	1.18	0.04	0.66	nd
Fe(m)	15.10	6.64	2.43	2.14	1.20	0.00	0.05	nd
Fe(m) σ	1.90	1.45	1.48	2.29	2.91	0.00	0.07	nd
Ni	1.66	1.22	0.98	1.41	1.21	1.10	1.26	1.05
Ni σ	0.13	0.12	0.23	0.27	0.54	0.24	0.10	nd
Co	0.08	0.06	0.05	0.07	0.06	0.06	0.07	0.06
Co σ	0.01	0.01	0.01	0.00	0.02	0.01	0.01	nd
FeS	5.27	5.71	5.61	5.42	5.13	2.83	7.70	9.08
FeS σ	0.61	0.98	1.14	2.74	0.93	0.56	1.71	nd
C	0.11	0.16	0.18	0.38	0.49	0.03	1.45	2.80
C σ	0.14	0.19	0.20	0.30	0.22	0.01	0.31	nd
NiO	74.69							
NiO σ	74.69							
CoO	74.93							
CoO σ	74.93							

Species	H	L	LL	CO	CV	CK	CM	CL
NiS	90.76							
NiS σ	90.76							
CoS	91.00							
CoS σ	91.00							
SO_3	80.06						1.62	5.88
SO_3 σ	80.06						0.66	nd
CO_2	44.01						0.92	1.50
CO_2 σ	44.01						0.39	nd

Table S-3 continued

Table S-4 Compositions of planetesimals cores determined by modelling metal/silicate segregation of averaged (Avg.) chondrite compositions from Jarosewich (2006). Uncertainties are propagated from uncertainties in averaged compositions for each group. Min. and Max. C refer to minimum and maximum C contents for petrological types 3-6, used to model how variability in C content within each group affects modelled core composition.

Chondrite Type	H			L			LL			CO			CM			CK			CV			CI		
	Min. C	Avg. C	Max. C	Min. C	Avg. C	Max. C	Min. C	Avg. C	Max. C	Min. C	Avg. C	Max. C	Min. C	Avg. C	Max. C	Min. C	Avg. C	Max. C	Min. C	Avg. C	Max. C	Min. C	Avg. C	Max. C
C input (wt. %)	0.01	0.16	1.08	0.01	0.18	0.88	0.06	0.38	0.80	N/A	1.45	N/A	0.03	0.03	0.06	0.25	0.49	1.12	N/A	2.80	N/A	0.01	0.16	1.08
Core Fe (wt. %)	75.17	74.35	69.69	65.83	64.61	59.38	61.36	59.25	56.70	N/A	44.17	N/A	44.63	44.63	44.41	56.56	54.94	50.95	N/A	37.56	N/A	75.17	74.35	69.69
Core Fe σ (wt. %)	15.33	15.13	14.05	22.59	22.05	19.87	38.87	37.26	35.38	N/A	11.16	N/A	10.43	10.43	10.37	44.76	43.20	39.53	N/A	N/A	N/A	15.33	15.13	14.05
Core Ni (wt. %)	8.93	8.83	8.28	10.81	10.61	9.75	15.50	14.97	14.32	N/A	11.23	N/A	27.34	27.34	27.20	15.39	14.95	13.86	N/A	6.81	N/A	8.93	8.83	8.28
Core Ni σ (wt. %)	1.48	1.46	1.35	3.39	3.31	2.97	6.44	6.11	5.74	/A	1.66	N/A	6.90	6.90	6.86	9.53	9.16	8.31	N/A	N/A	N/A	1.48	1.46	1.35
Core S (wt. %)	15.11	14.95	14.04	22.18	21.79	20.08	21.43	20.73	19.87	N/A	30.69	N/A	24.75	24.75	24.64	23.39	22.75	21.16	N/A	36.78	N/A	15.11	14.95	14.04
Core S σ (wt. %)	6.86	6.93	7.49	10.45	10.37	10.40	20.27	20.30	20.57	N/A	8.65	N/A	6.68	6.68	6.66	21.62	21.45	21.72	N/A	N/A	N/A	6.86	6.93	7.49
Core C (wt. %)	0.07	1.16	7.33	0.11	1.94	9.81	0.66	4.03	8.12	N/A	12.96	N/A	0.75	0.75	1.24	3.30	6.03	12.79	N/A	18.23	N/A	0.07	1.16	7.33
Core C σ (wt. %)	0.01	0.15	0.95	0.02	0.39	1.87	0.24	1.45	2.86	N/A	1.61	N/A	0.09	0.09	0.15	1.41	2.53	5.10	N/A	N/A	N/A	0.01	0.15	0.95
Core P (wt. %)	0.72	0.71	0.67	1.08	1.06	0.97	1.05	1.02	0.97	N/A	0.95	N/A	2.53	2.53	2.52	1.37	1.33	1.23	N/A	0.63	N/A	0.72	0.71	0.67
Core P σ (wt. %)	0.15	0.15	0.14	0.34	0.34	0.30	0.40	0.37	0.35	N/A	0.18	N/A	0.32	0.32	0.31	0.65	0.62	0.55	N/A	N/A	N/A	0.15	0.15	0.14

Supplementary Figures

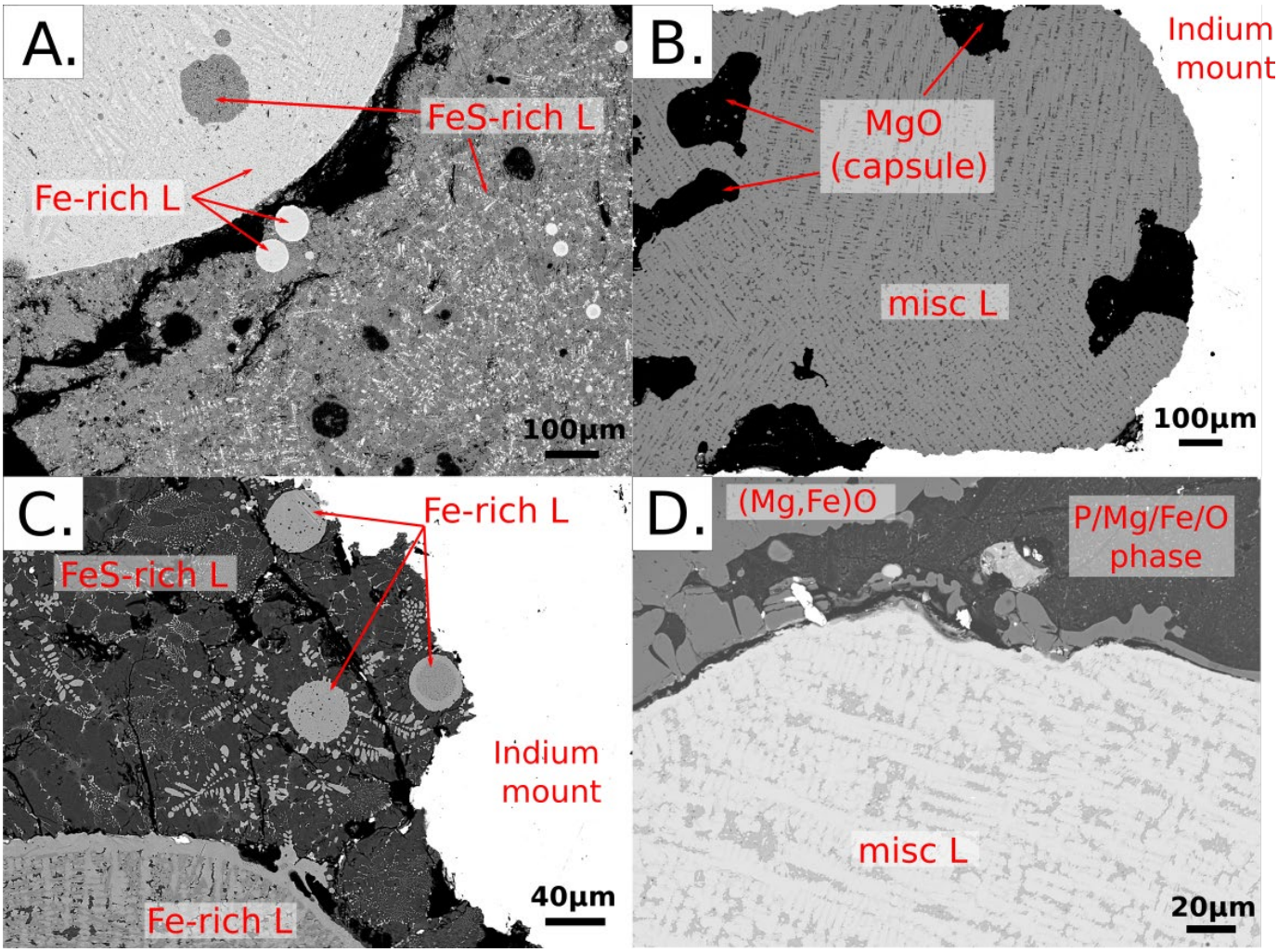

Figure S-1 continued overleaf

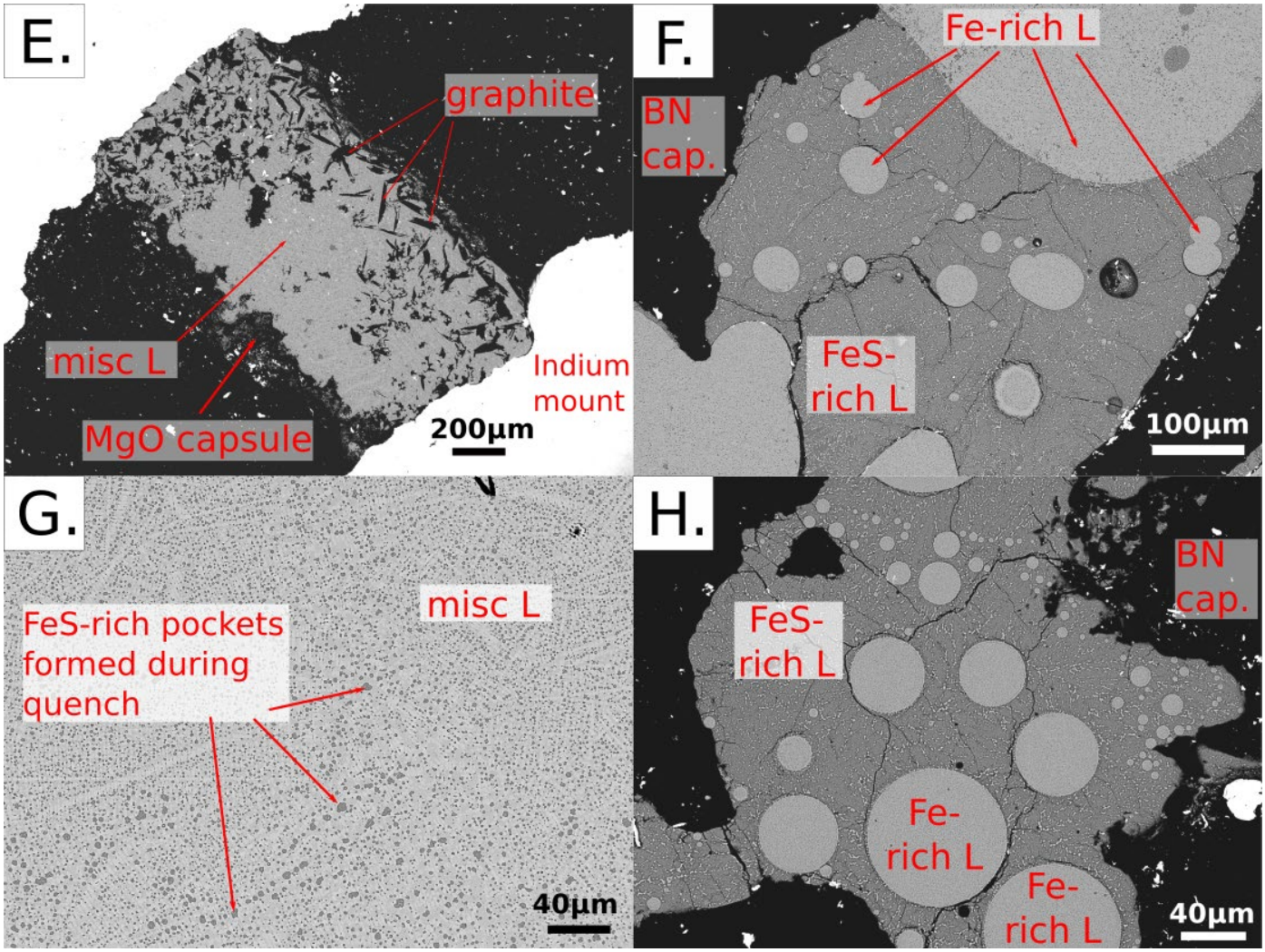

Figure S-1 Backscattered electron images of selected run products showing typical textures. A. IM_7, showing extensive but incomplete segregation of immiscible Fe-rich and FeS-rich liquids, and coarse exsolution textures coarse exsolution textures, both characteristic of experiments performed in graphite capsules. Black regions are holes. B. IM_12 showing exsolution in a single miscible liquid in an MgO capsule experiment. Limited melt percolation into MgO capsule is observed. C. IM_19 showing complex quench textures, especially in quenched FeS-rich liquid, typical of experiments in MgO capsules. Darker grey areas are holes. D. IM_21, showing examples of sample/MgO capsule reactions. Light grey area is (Mg,Fe)O, with approximately 50 wt. % Fe. Dark grey regions are mixed phase, dominantly MgO with lower Fe contents (≈15 wt. % Fe), but enriched in P (15 wt. % P). E. IM_23 showing coarse exsolution textures in miscible liquid with minor reaction and melt percolation into the surrounding MgO capsule. Acicular black phases are graphite crystals (distinct from irregular black holes in the polished section), implying C saturation. F. IM_24B showing finer exsolution textures characteristic of experiments in hBN capsules. Less-developed phase segregation is also characteristic of hBN capsule experiments. Note frozen textures showing coalescence of near-spherical regions of Fe-rich liquid. G. IM_28A showing finer scale exsolution in quenched miscible liquid in hBN capsules. Darker grey regions are small pockets of FeS-rich phases formed during quenching/exsolution which are typically an order of magnitude smaller than in MgO capsule experiments. H. IM_28B showing less developed segregation of immiscible liquids in hBN capsules, even after protracted run durations. However, in longer duration experiments complete separation into immiscible spheres is noted, in contrast to presence of FeS-rich liquid blobs within Fe-rich liquid blobs seen in F.

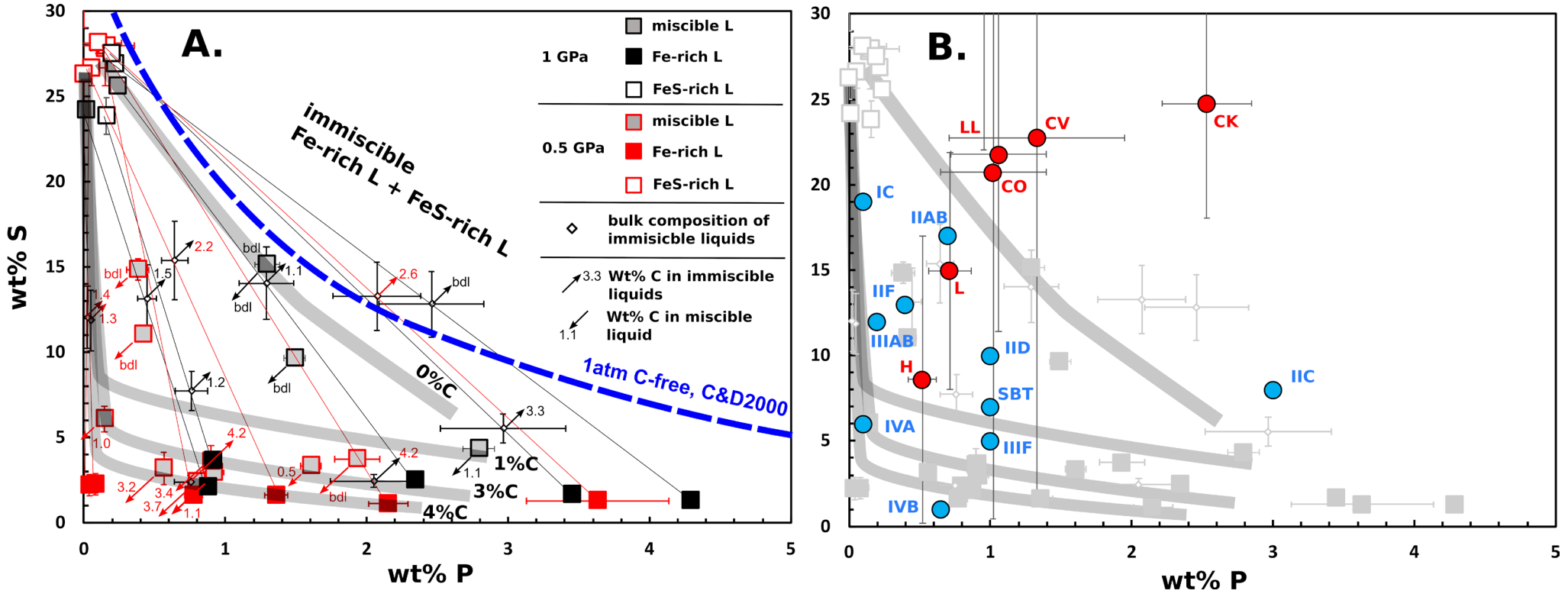

Figure S-2 A. Liquid compositions in the system $Fe_{0.9}Ni_{0.1}$,S,P,C,O at 0.5 (red)/1.0 GPa (black), and calculated bulk compositions for immiscible liquids. Tie-lines connect compositions of coexisting immiscible liquids. Small numbers are wt. % C in run products, for miscible liquids (i.e. direct measurements of C content; arrows pointing to bottom left), and for immiscible liquids (i.e. calculated bulk C composition for both liquids, based on visually estimated phase proportions; arrows pointing to top right). Thick grey lines are inferred position of miscibility curve as a function of bulk C content. Blue, dashed line is the miscibility curve from Chabot and Drake (2000), based on their experiments conducted in the system Fe/Ni-S-P (C-free) in evacuated silica tubes (nominally 1 atmosphere) at 1050-1400 °C. B. Model core-forming liquid compositions (from Figure 2) superimposed onto experimental data, and inferred miscibility fields, from this study. Data from this study shown in light grey for clarity. Blue circles: Iron meteorite parent body compositions (Hilton *et al.*, 2022). Red circles: modelled planetesimal core compositions based on metal/silicate differentiation of averaged chondrite compositions, after the method of Bercovici *et al*. (2022). Error bars are propagated from uncertainties in S and P contents in averaged chondrite data.

Supplementary Information References

Bercovici, H.L., Elkins-Tanton, L.T., O'Rourke, J.G., Schaefer, L. (2022) The effects of bulk composition on planetesimal core sulfur content and size. *Icarus* 380, 114976. https://doi.org/10.1016/j.icarus.2022.114976

Berg, M.T.L., Bromiley, G.D., Le Godec, Y., Philippe, J., Mezouar, M., Perrillat, J.-P., Potts, N.J. (2018) Rapid core formation in terrestrial planets by percolative flow: In-situ imaging of metallic melt migration under high pressure/temperature conditions. *Frontiers in Earth Science* 6. https://doi.org/10.3389/feart.2018.00077

Bromiley, G.D. (2023) The Geochemical Legacy of Low-Temperature, Percolation-Driven Core Formation in Planetesimals. *Earth, Moon, and Planets* 127, 4. https://doi.org/10.1007/s11038-023-09552-2

Chabot, N.L., Drake, M.J. (2000) Crystallization of magmatic iron meteorites: The effects of phosphorus and liquid immiscibility. Meteoritics and Planetary Science 35, 807–816. https://doi.org/10.1111/j.1945-5100.2000.tb01464.x

Corgne, A., Wood, B.J., Fei, Y. (2008) C- and S-rich molten alloy immiscibility and core formation of planetesimals. *Geochimica et Cosmochimica Acta* 72, 2409–2416. https://doi.org/10.1016/j.gca.2008.03.001

Dasgupta, R., Walker, D. (2008) Carbon solubility in core melts in a shallow magma ocean environment and distribution of carbon between the Earth's core and the mantle. *Geochimica et Cosmochimica Acta* 72, 4627–4641. https://doi.org/10.1016/j.gca.2008.06.023

Dasgupta, R., Buono, A., Whelan, G., Walker, D. (2009) High-pressure melting relations in Fe-C-S systems: Implications for formation, evolution, and structure of metallic cores in planetary bodies. *Geochimica et Cosmochimica Acta* 73, 6678–6691. https://doi.org/10.1016/j.gca.2009.08.001

Goldstein, J.I., Scott, E.R.D., Chabot, N.L. (2009) Iron meteorites: Crystallization, thermal history, parent bodies, and origin. Geochemistry 69, 293–325. https://doi.org/10.1016/j.chemer.2009.01.002

Grewal, D.S., Dasgupta, R., Sun, C., Tsuno, K., Costin, G. (2019a) Delivery of carbon, nitrogen, and sulfur to the silicate Earth by a giant impact. *Science Advances 5, eaau3669.* https://doi.org/10.1126/sciadv.aau3669

Grewal, D.S., Dasgupta, R., Holmes, A., Costin, G., Li, Y., Tsuno, K. (2019b) The fate of nitrogen during core-mantle separation on Earth. *Geochimica et Cosmochimica Acta* 251, 87–115. https://doi.org/10.1016/j.gca.2019.02.009

Grewal, D.S., Asimow, P.D. (2023) Origin of the superchondritic carbon/nitrogen ratio of the bulk silicate Earth – an outlook from iron meteorites. *Geochimica et Cosmochimica Acta* 344, 146–159. https://doi.org/10.1016/j.gca.2023.01.012

Grewal, D.S., Nie, N.X., Zhang, B., Izidoro, A., Asimow, P.D. (2024) Accretion of the earliest inner Solar System planetesimals beyond the water snowline. *Nature Astronomy* 8, 290–297. https://doi.org/10.1038/s41550-023-02172-w

Gu, T., Stagno, V., Fei, Y. (2019) Partition coefficient of phosphorus between liquid metal and silicate melt with implications for the Martian magma ocean. *Physics of the Earth and Planetary Interiors* 295, 106298. https://doi.org/10.1016/j.pepi.2019.106298

Hezel, D. (2020) MetBase.org as a Research and Learning Tool for Cosmochemistry. *Elements* 16, 73–75. https://doi.org/10.2138/gselements.16.1.73

Hilton, C.D., Ash, R.D., Walker, R.J. (2022) Chemical characteristics of iron meteorite parent bodies. *Geochimica et Cosmochimica Acta* 318, 112–125. https://doi.org/10.1016/j.gca.2021.11.035

Hirschmann, M.M., Bergin, E.A., Blake, G.A., Ciesla, F.J., Li, J. (2021) Early volatile depletion on planetesimals inferred from C-S systematics of iron meteorite parent bodies. *Proceedings of the National Academy of Sciences* 118, e2026779118. https://doi.org/10.1073/pnas.2026779118

Hunt, A.C., Theis, K.J., Rehkämper, M., Benedix, G.K., Andreasen, R., Schönbächler, M. (2022) The dissipation of the solar nebula constrained by impacts and core cooling in planetesimals. *Nature Astronomy* 6, 812–818. https://doi.org/10.1038/s41550-022-01675-2

Jarosewich, E. (2006) Chemical analyses of meteorites at the Smithsonian Institution: An update. *Meteoritics and Planetary Science* 41, 1381–1382. https://doi.org/10.1111/j.1945-5100.2006.tb00528.x

Kaminski, E., Limare, A., Kenda, B., Chaussidon, M. (2020) Early accretion of planetesimals unraveled by the thermal evolution of the parent bodies of magmatic iron meteorites. *Earth and Planetary Science Letters* 548, 116469. https://doi.org/10.1016/j.epsl.2020.116469

Keppler, H., Golabek, G. (2019) Graphite floatation on a magma ocean and the fate of carbon during core formation. *Geochemical*

Perspectives Letters 11, 12–17. https://doi.org/10.7185/geochemlet.1918

Lichtenberg, T., Keller, T., Katz, R.F., Golabek, G.J., Gerya, T.V. (2019) Magma ascent in planetesimals: control by grain size. *Earth and Planetary Science Letters* 507, 154-165. https://doi.org/10.1016/j.epsl.2018.11.034

Mare, E.R., Tomkins, A.G., Godel, B.M. (2014) Restriction of parent body heating by metal-troilite melting: Thermal models for the ordinary chondrites. *Meteoritics and Planetary Science* 49, 636–651. https://doi.org/10.1111/maps.12280

Matthes, M., Fischer-Gödde, M., Kruijer, T.S., Kleine, T. (2018) Pd-Ag chronometry of IVA iron meteorites and the crystallization and cooling of a protoplanetary core. *Geochimica et Cosmochimica Acta* 220, 82–95. https://doi.org/10.1016/j.gca.2017.09.009

Melwani Daswani, M., Vance, S.D., Mayne, M.J., Glein, C.R. (2021) A Metamorphic Origin for Europa's Ocean. *Geophysical Research Letters* 48, e2021GL094143. https://doi.org/10.1029/2021GL094143

Potts, N.J., Bromiley, G.D., Brooker, R.A. (2021) An experimental investigation of F, Cl and H_2O mineral-melt partitioning in a reduced, model lunar system. *Geochimica et Cosmochimica Acta* 294, 232–254. https://doi.org/10.1016/j.gca.2020.12.003

Sturtz, C., Limare, A., Tait, S., Kaminski, E. (2022) Birth and Decline of Magma Oceans in Planetesimals: 2.Structure and Thermal History of Early Accreted Small Planetary Bodies. *Journal of Geophysical Research: Planets* 127, e2021JE007020. https://doi.org/10.1029/2021JE007020

Trinh, K.T., Bierson, C.J., O'Rourke, J.G. (2023) Slow evolution of Europa's interior: metamorphic ocean origin, delayed metallic core formation, and limited seafloor volcanism. *Science Advances* 9, eadf3955. https://doi.org/10.1126/sciadv.adf3955

Yang, J., Goldstein, J.I., Scott, E.R.D. (2007) Iron meteorite evidence for early formation and catastrophic disruption of protoplanets. *Nature* 446, 888–891. https://doi.org/10.1038/nature05735

Yang, J., Goldstein, J.I., Scott, E.R.D. (2010) Main-group pallasites: Thermal history, relationship to IIIAB irons, and origin. *Geochimica et Cosmochimica Acta* 74, 4471–4492. https://doi.org/10.1016/j.gca.2010.04.016

Zhai, K., Yin, Y., Zhai, S. (2022) New constraints on the abundances of phosphorus and sulfur in the lunar core: High-pressure and high-temperature experimental study of the FeSP ternary system. *Geochimica et Cosmochimica Acta* 334, 1–13. https://doi.org/10.1016/j.gca.2022.07.024

Zhang, Z., Hastings, P., Von der Handt, A., Hirschmann, M.M. (2018) Experimental determination of carbon solubility in Fe-Ni-S melts. *Geochimica et Cosmochimica Acta* 225, 66–79. https://doi.org/10.1016/j.gca.2018.01.009